

Supplementary Information

Atomic-Thin Hexagonal CuCo Nanocrystals with *d*-Band Tuning for CO₂ Reduction

Yibo Yan,^{a} Zhengping Zhao,^b Jun Zhao,^c Wenfei Tang,^a Wei Huang,^{a*} and Jong-Min Lee,^{*c}*

^aFrontiers Science Center for Flexible Electronics, Xi'an Institute of Flexible Electronics (IFE) and Xi'an Institute of Biomedical Materials & Engineering, Northwestern Polytechnical University, 127 West Youyi Road, Xi'an 710072, China

^bZhijiang College, Zhejiang University of Technology, Hangzhou, Zhejiang 310014, China

^cSchool of Chemical and Biomedical Engineering, Nanyang Technological University, 62 Nanyang Drive, 637459, Singapore

Email:

Yibo Yan: iamybyan@nwpu.edu.cn

Wei Huang: iawhuang@nwpu.edu.cn

Jong-Min Lee: jmlee@ntu.edu.sg

Table of contents

Material synthesis	3
Characterizations	4
Electrochemical experiments	4
Computation methods	5
Fig. S1	6
Fig. S2	7
Fig. S3	8
Fig. S4	9
Fig. S5	9
Fig. S6	10
Fig. S7	10
Fig. S8	11
Table S1	11
Fig. S9	12
Fig. S10	12
Fig. S11	13
Fig. S12	14
Fig. S13	14
Fig. S14	15
References	16

Material synthesis

Atomic-layered hexagonal CuCo nanocrystals: 2 mmol of cobalt acetylacetonate (10.7 mg) in DMF solution (15 mL) was mixed with 2 mmol of copper acetylacetonate (7.9 mg) in DMF solution (15 mL). 5 mL of de-ionized water and 76mg of 2-aminopyrene as the ligand for metal were added into the mixture. After magnetic stirring and ultrasonication for 30 min, the mixture was transferred into a 50-mL Teflon-lined autoclave. The sealed autoclave was located in 130 °C of oven and heated for 3 h. Then it was cooled down to room temperature after the reaction. Toluene and ethanol were used to rinse the sample for several times with centrifugation separation. The final product was preserved in ethanol to make a liquid phase protection.

Cu₃Co, Cu₂Co, CuCo₂, CuCo₃ nanocrystals: The above steps were replaced, while the precursor amount was replaced by 1 mmol of cobalt acetylacetonate in DMF solution and 3 mmol of copper acetylacetonate in DMF solution for the preparation of Cu₃Co.

For preparation of Cu₂Co, the above steps were replaced, while the precursor amount was replaced by 1 mmol of cobalt acetylacetonate in DMF solution and 2 mmol of copper acetylacetonate in DMF solution.

For the preparation of CuCo₂, the above steps were replaced, while the precursor amount was replaced by 2 mmol of cobalt acetylacetonate in DMF solution and 1 mmol of copper acetylacetonate in DMF solution.

For preparation of CuCo₃, the above steps were replaced, while the precursor amount was replaced by 3 mmol of cobalt acetylacetonate in DMF solution and 1 mmol of

copper acetylacetonate in DMF solution.

Characterizations

Transmission electron microscopy (TEM) and atomic force microscopy (AFM) were performed on the JEOL JEM 2100F and Bruker ICON AFM, respectively. Elemental mapping was recorded by the energy-dispersive X-ray spectroscopy (EDX) on JEOL JEM 2100 F. X-ray diffraction (XRD) pattern was obtained from Bruker AXS D8 diffractometer armed with a filtered CuK α radiation ($\lambda = 0.15406$ nm) source at 40 mA, 40 kV. X-ray photoelectron spectroscopy (XPS) and Ultraviolet photoelectron spectroscopy (UPS) spectra were recorded by Kratos Axis Ultra DLD. The XPS spectra were obtained using the Al K-Alpha radiation ($h\nu = 1486.6$ eV) source at the accelerating voltage of 13 kV, and UPS spectra were collected using He (I) laser source. High-angle annular dark-field scanning transmission electron microscopy (HAADF-STEM) was performed on a FEI Tecnai F20 TEM with accelerating voltage at 200 kV. The metallic components are measured by inductively coupled plasma (ICP) of PerkinElmer Avio 500. And the X-ray absorption near edge structure (XANES) and extended X-ray absorption fine structure (EXAFS) were conducted on QuantumLeap X-ray absorption spectroscopy with synchrotron-like performance (Sigray). Diffuse reflectance infrared Fourier transform spectroscopy (DRIFTS) were conducted by Thermo Scientific Nicolet 6700 spectrometer armed with Harrick Praying Mantis reaction chamber and mercury cadmium telluride (MCT-A) detector.

Electrochemical experiments

A two-compartment H-type cell with an isolating NAFION N117 ion exchange

membrane, and an CHI760E work-station were used for all electrochemical tests including electrochemical impedance spectroscopy. A Pt foil was employed as counter electrode in anode cell, while sample-covered glassy carbon electrode and Ag/AgCl electrode were employed as working and reference electrodes, respectively in cathode cell. To prepare the catalyst ink, 10 mg of sample was evenly dispersed in 0.5 mL of 5% Nafion ethanol solution. 50 μ L of catalyst ink was gradually dropped and dried on a glassy carbon electrode as the working electrode. The CO₂ electrocatalytic reduction was carried out in a CO₂-saturated 0.5 M KHCO₃ electrolyte. CO₂ was purged into KHCO₃ electrolyte for 1 h to ensure saturation and remove residual air. The potential controlled electrolysis was conducted for 4 h at each potential. Gaseous phase of cathode cell was connected to online gas chromatograph (GC, Agilent 6890N-G1540N) with a thermal conductivity detector (TCD), a Porapak Q column and a Molecular Sieve 5A column to analyze gas products. Liquid phase was analyzed by Agilent LC-MS 6130. All potentials were measured using Ag/AgCl reference electrode and converted to the RHE reference *via* $E(\text{vs. RHE}) = E(\text{vs. Ag/AgCl}) + 0.21 \text{ V} + 0.0591 \times \text{pH}$.

Computation methods

Density functional theory (DFT) using a Vienna ab initio simulation package (VASP)¹ together with Perdew–Burke–Ernzerhof (PBE)² have been employed. A DFT Semi-core Pseudo-potential (DSPP) was set as core treatment to maintain balance between the efficiency and accuracy of computation. And double numerical plus polarization was set as the basis set. Brillouin zone was sampled using the 2 \times 2 \times 1 Monkhorst-Pack point³. Gaussian smearing technique (default smearing width of 0.005 Ha) was

applied to accelerate convergence. Self-consistent-field (SCF) convergence criteria were set 1.0×10^{-6} Ha. Energy convergence criteria were set as 2.0×10^{-5} Ha. The maximum force convergence criteria were set as 0.004 Ha/Å, and the maximum displacement criteria were set as 0.005 Å. The Cu-Co surface was modeled as two-layer slab with (4×4) unit cells. Vacuum spacing of 15 Å was set, vertically separating the slabs. Gibbs free energy changes were obtained in a proton-coupled electron transfer (PCET) process using a well-recognized computational hydrogen electrode (CHE) model⁴. Zero-point energies (ZPE) and the vibrational influence on entropy for distinct adsorbates were considered within a well-constructed harmonic oscillator approximation⁵.

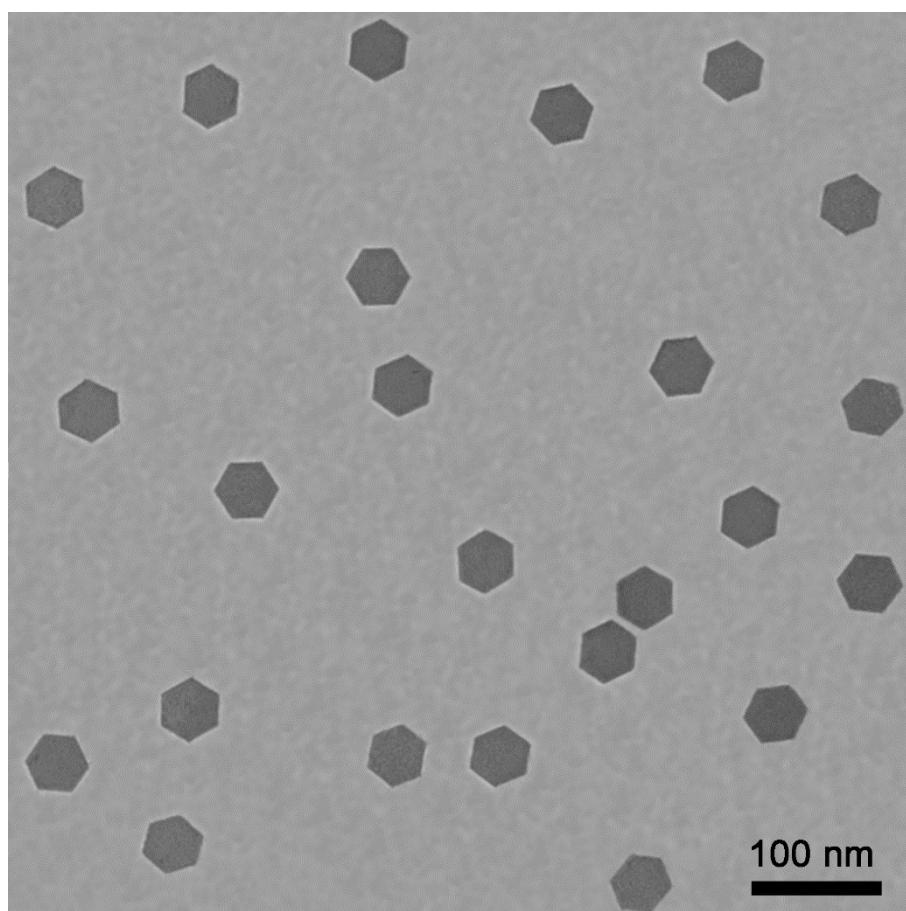


Fig. S1 TEM characterization of the Cu_3Co nanocrystal sample.

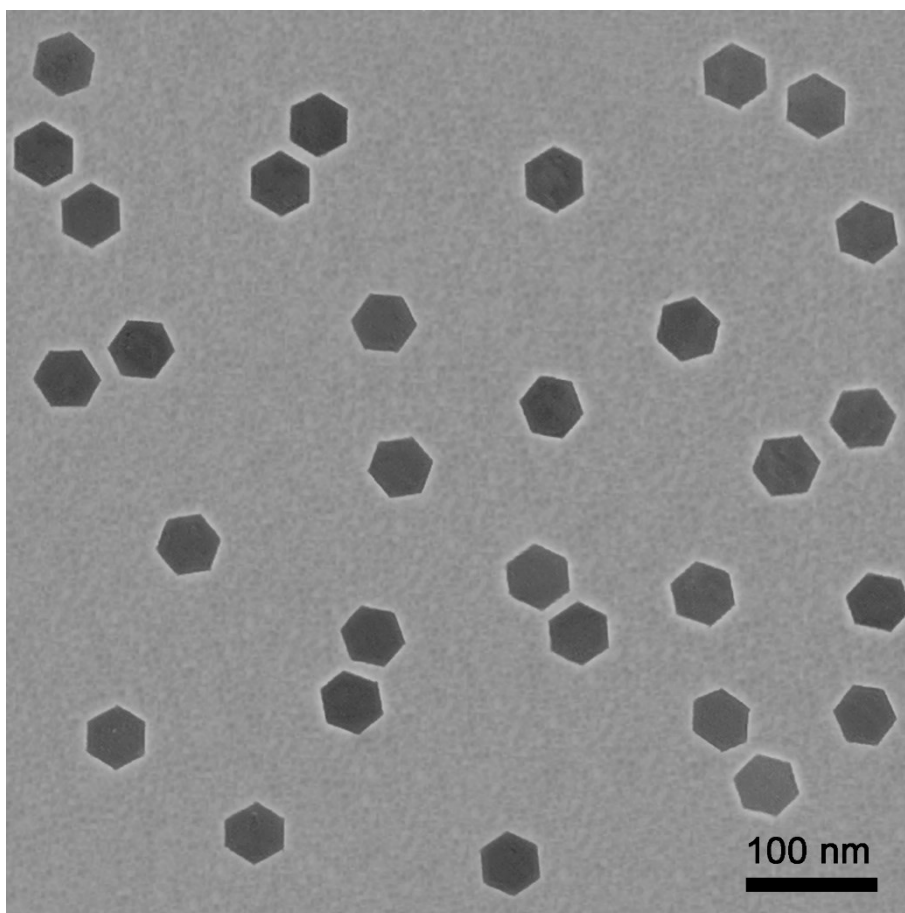


Fig. S2 TEM characterization of the Cu₂Co nanocrystal sample.

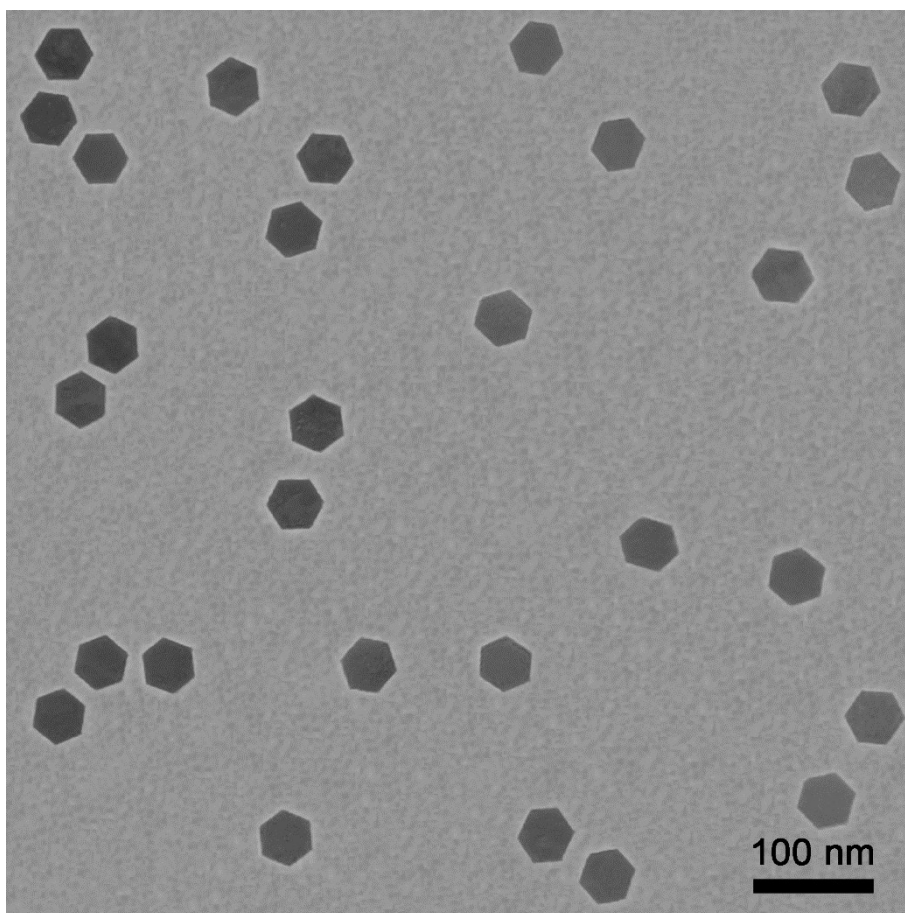


Fig. S3 TEM characterization of the CuCo₂ nanocrystal sample.

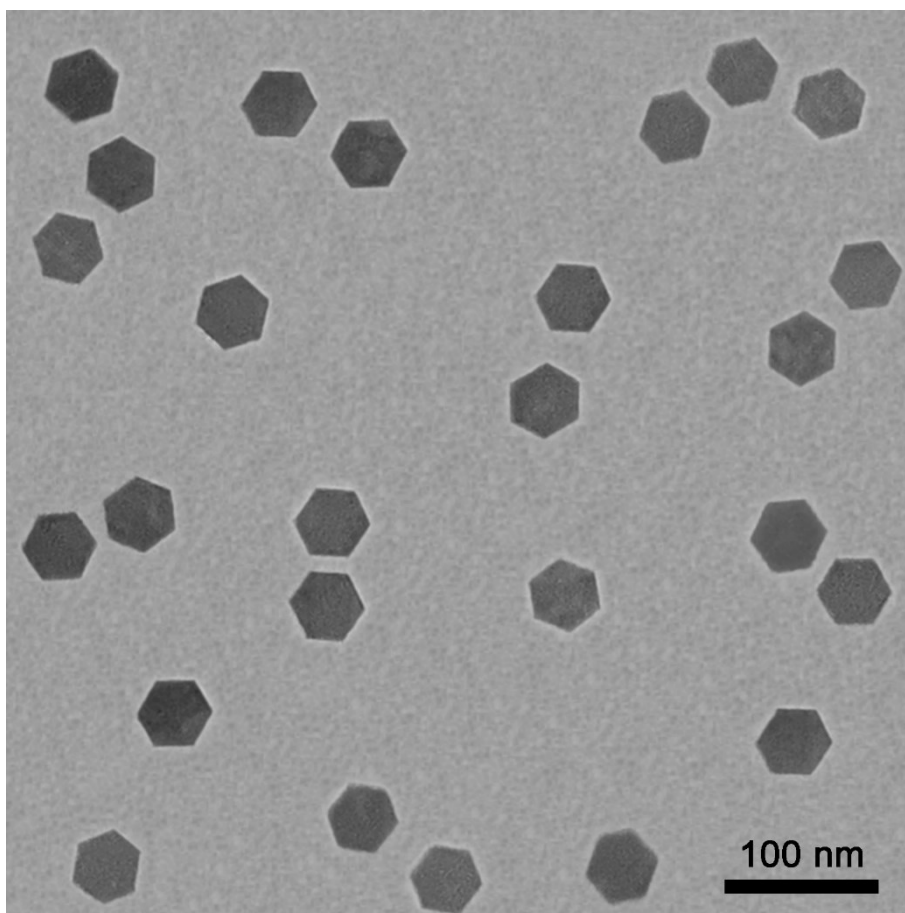


Fig. S4 TEM characterization of the CuCo_3 nanocrystal sample.

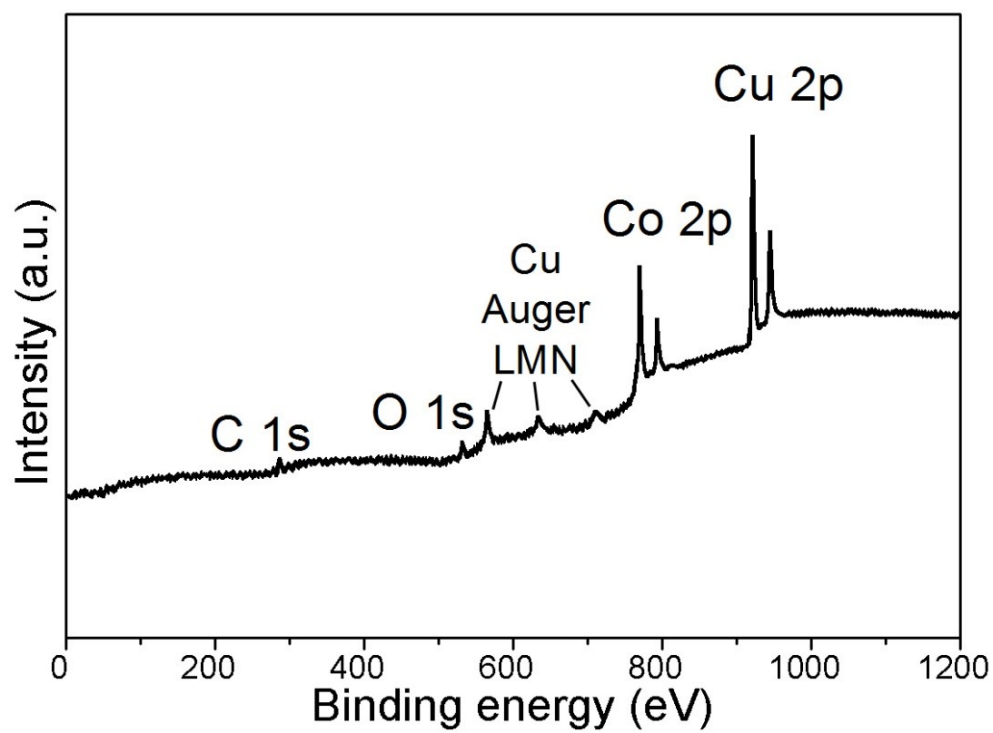


Fig. S5 Overall XPS spectrum of the CuCo nanocrystals.

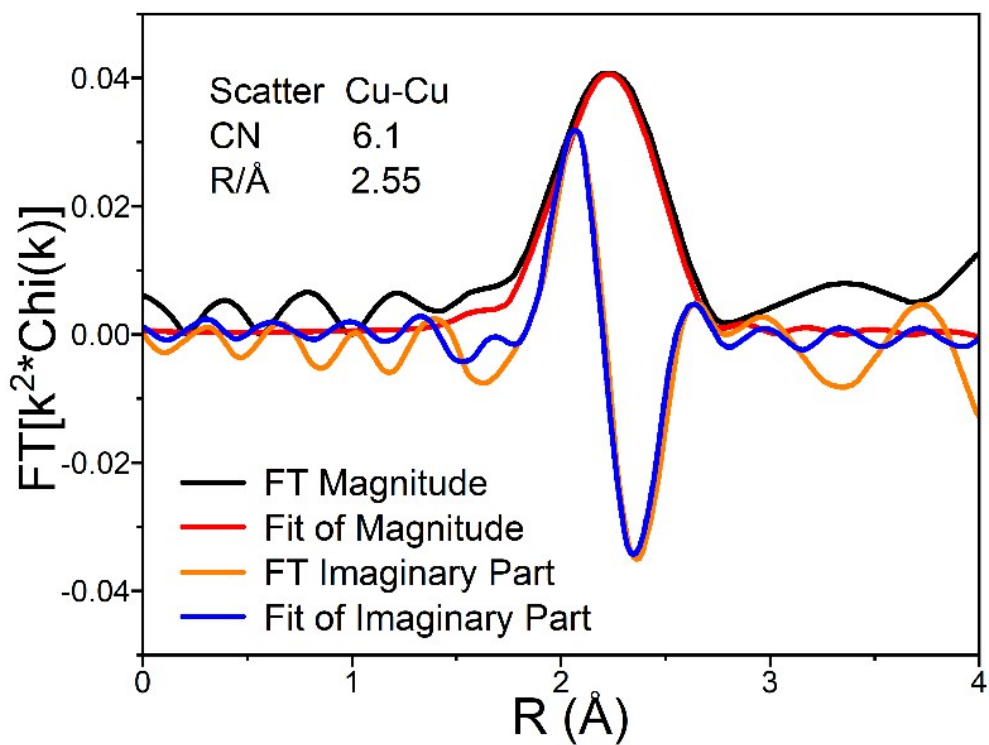


Fig. S6 k^2 -weighted R-space EXAFS spectra of Cu-Cu bond in CuCo nanosheets. CN denotes the coordination number.

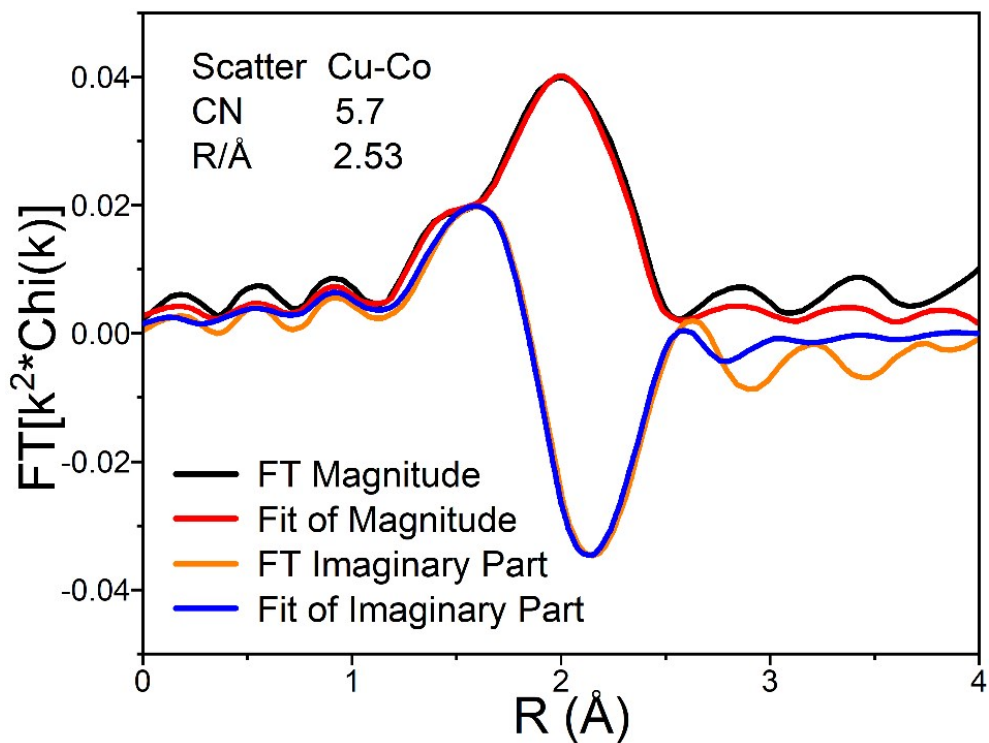


Fig. S7 k^2 -weighted R-space EXAFS spectra of Cu-Co bond in CuCo nanosheets. CN denotes the coordination number.

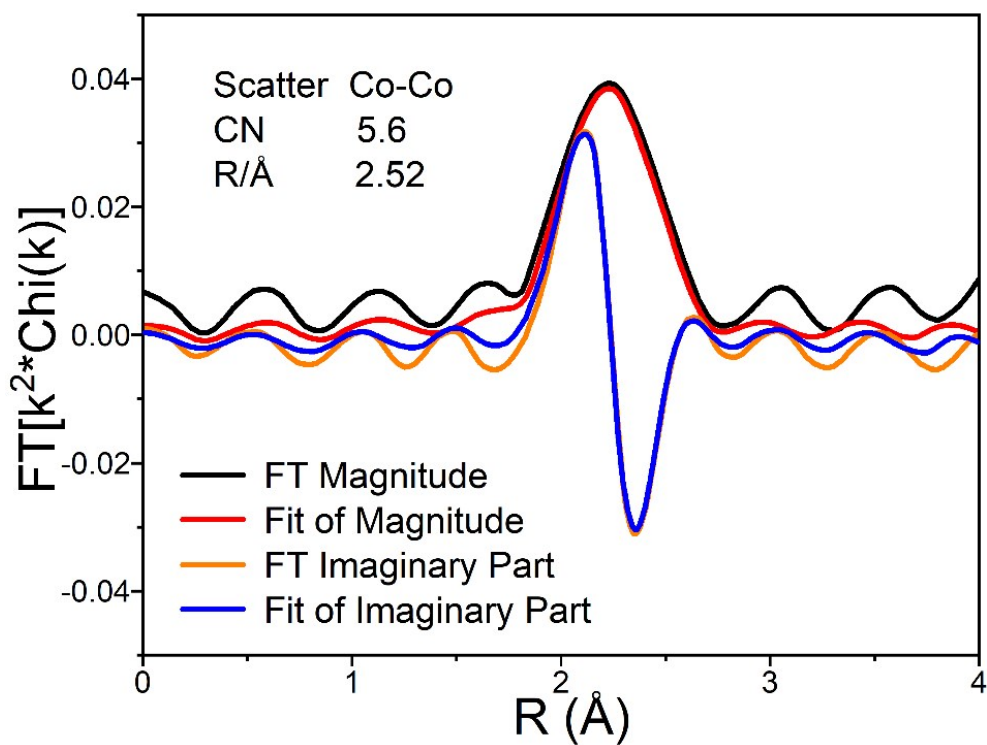


Fig. S8 k^2 -weighted R-space EXAFS spectra of Co-Co bond in CuCo nanosheets. CN denotes the coordination number.

Table S1 EXAFS fitting results of Cu-Co bimetallic nanocrystals from Fig. S6-S8.

Scatter	CN	R, Å	$\Delta\sigma^2$	ΔE_0 , eV
Cu-Cu	6.1	2.55	0.64	-0.32
Cu-Co	5.7	2.53	1.98	-0.17
Co-Co	5.6	2.52	0.83	-0.29

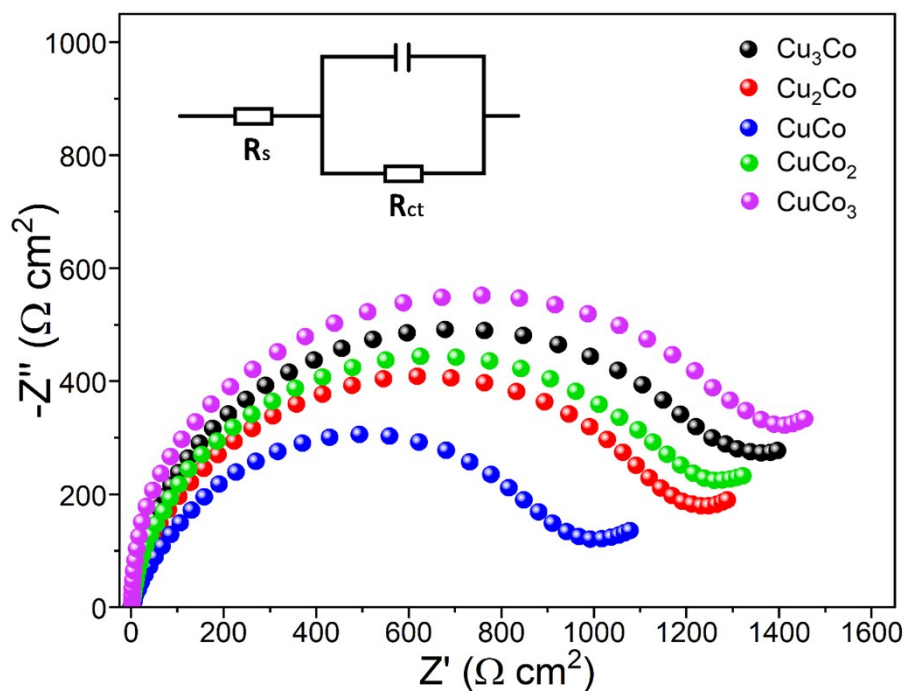


Fig. S9 The electrochemical impedance spectra (EIS) diagrams with Nyquist plots representation for each catalyst. The smallest radius of CuCo implies the smallest charge transfer resistance (i.e., the highest charge transfer speed).

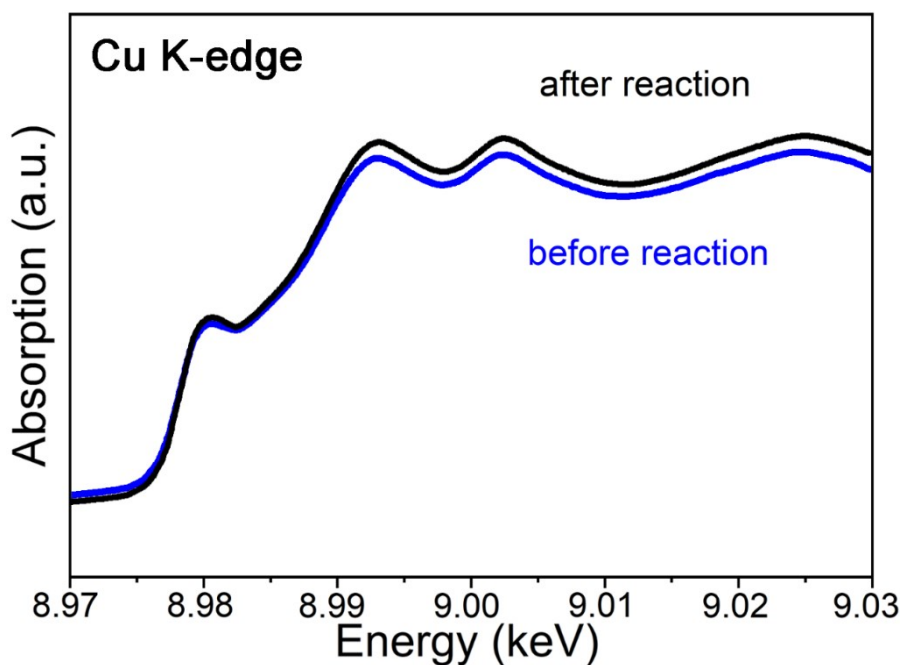


Fig. S10 The Cu K-edge XANES spectra of CuCo catalyst before and after reaction. The good stability of the catalyst without change in Cu^0 valance states is ascribed to the reductive reaction condition and fast electron transfer process.

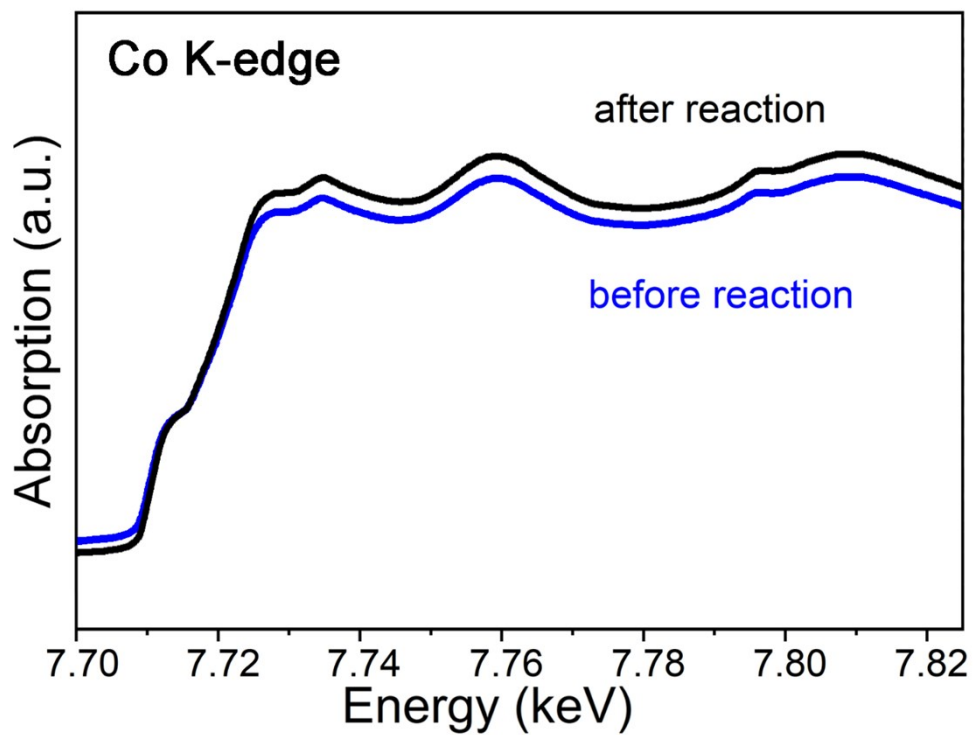


Fig. S11 The Co K-edge XANES spectra of CuCo catalyst before and after reaction. The good stability of the catalyst without change in Co^0 valance states is ascribed to the reductive reaction condition and fast electron transfer process.

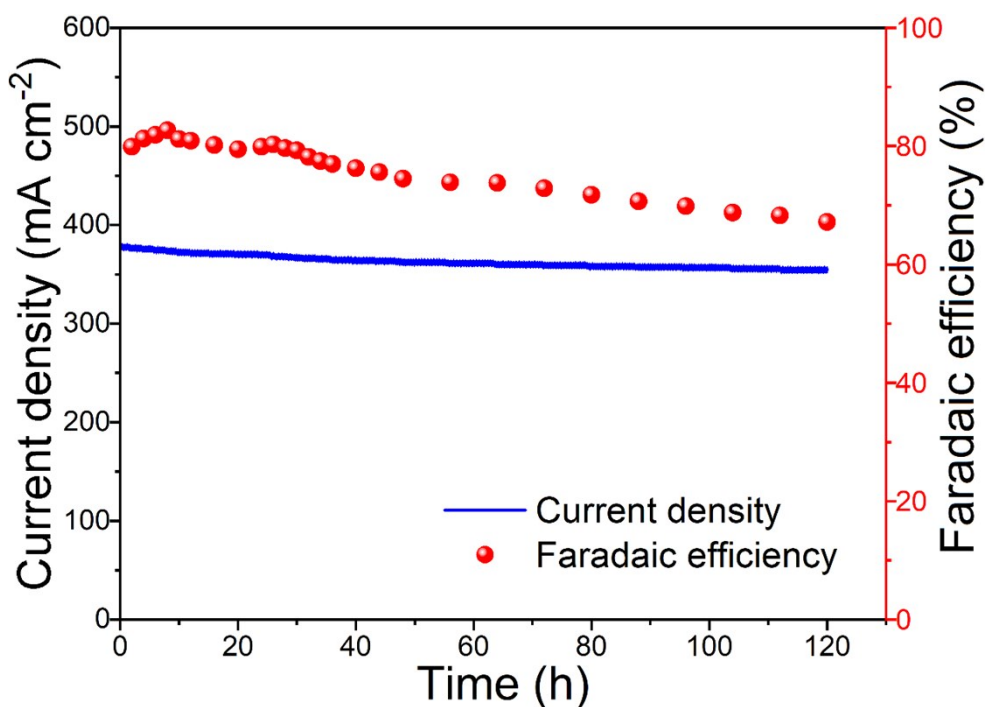


Fig. S12 Faradaic efficiency for C_2H_4 (red ball) and total current density (blue line) using CuCo electrocatalyst for a much longer electrolysis (120 h).

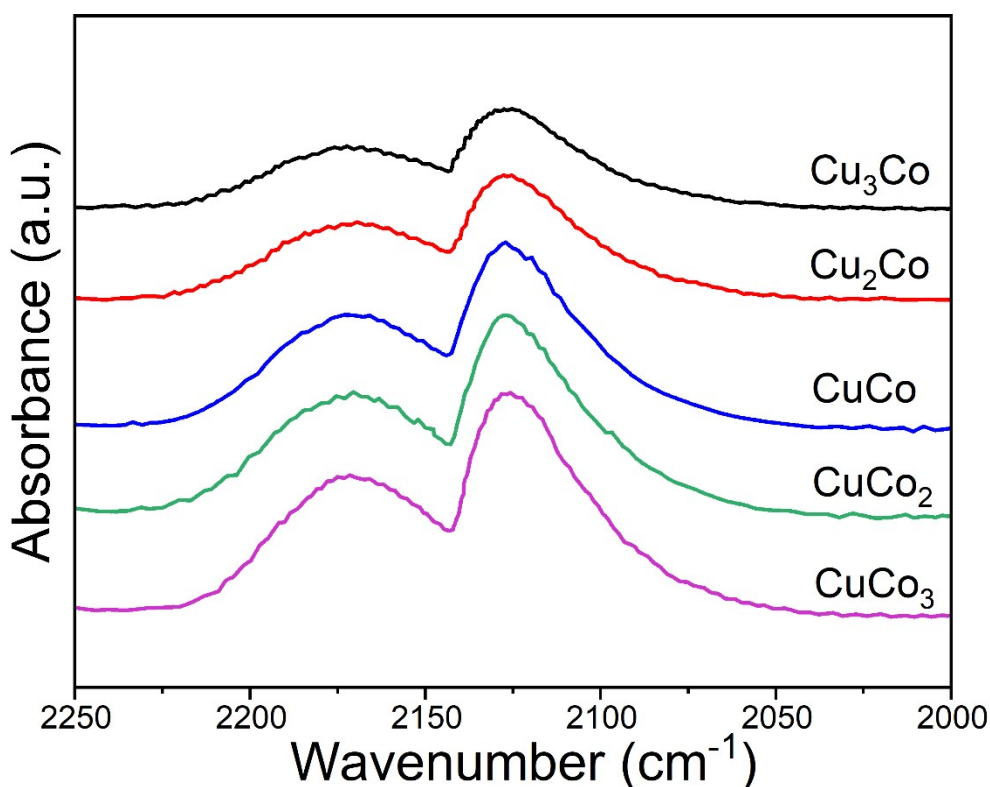


Fig. S13 *In situ* CO-DRIFT of the different electrocatalysts at room temperature. It implies the increasing of Co content can increase the CO adsorption energy. Among these samples, CuCo possesses the appropriately enhanced CO adsorption.

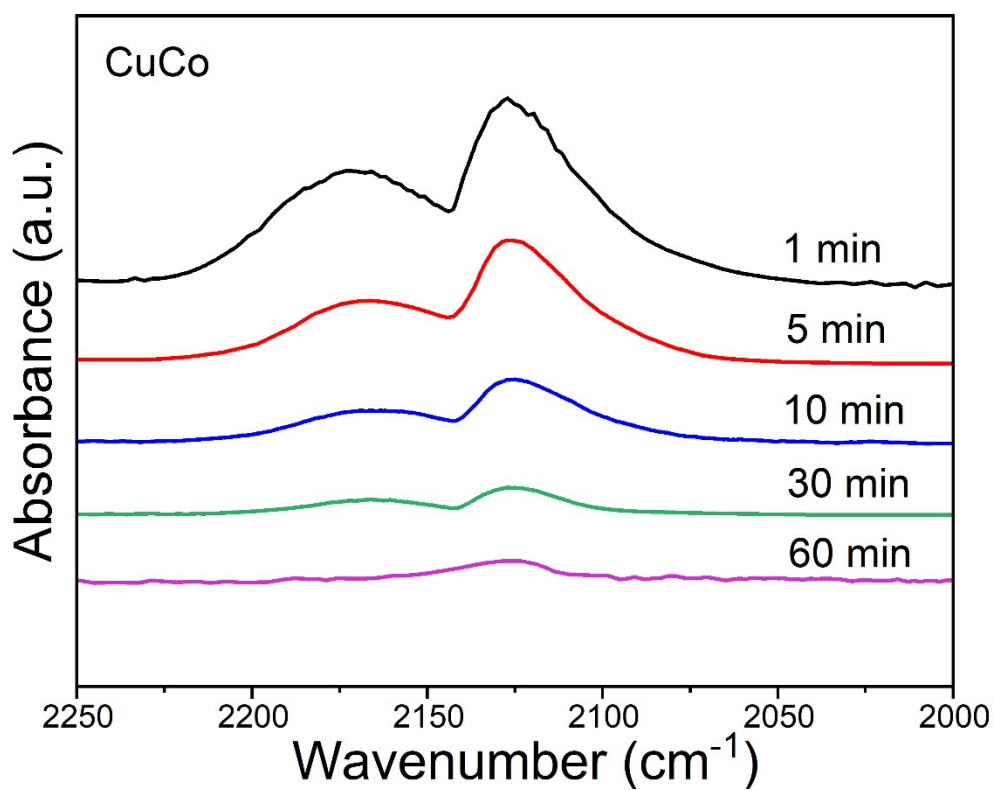


Fig. S14 *In situ* CO-DRIFT of the CuCo catalyst with the spontaneous CO desorption for 1, 5, 10, 30 and 60 min at room temperature. It demonstrates the good adsorption-desorption efficiency of CuCo, which avoids the CO over-binding

References

1. G. Kresse and J. Furthmuller, *Physical Review B*, 1996, **54**, 11169-11186.
2. J. P. Perdew, K. Burke and M. Ernzerhof, *Physical Review Letters*, 1996, **77**, 3865-3868.
3. H. J. Monkhorst and J. D. Pack, *Physical Review B*, 1976, **13**, 5188-5192.
4. J. K. Nørskov, J. Rossmeisl, A. Logadottir, L. Lindqvist, J. R. Kitchin, T. Bligaard and H. Jónsson, *The Journal of Physical Chemistry B*, 2004, **108**, 17886-17892.
5. M. S. Xie, B. Y. Xia, Y. Li, Y. Yan, Y. Yang, Q. Sun, S. H. Chan, A. Fisher and X. Wang, *Energy & Environmental Science*, 2016, **9**, 1687-1695.